*J. Fluid Mech.* (1970), *vol.* 40, *part* 3, *pp.* 495–511
*Printed in Great Britain*



# Experiments on liquid jet instability

By E. F. GOEDDE
Westinghouse Corporation, Sunnyvale, California
AND M. C. YUEN
Northwestern University, Evanston, Illinois

(Received 25 March and in revised form 17 July 1969)

The capillary instability of vertical liquid jets of different viscosities have been examined by imposing audio-frequency disturbances. Real time sequences of photographs allow a direct measurement of growth rates of disturbances of various wavelengths. Results show that in general non-linear effects dominate the growth processes. This is in agreement with Yuen's analysis. The growth rate of the difference between the neck and the swell, however, agrees well with the linearized analysis of Rayleigh and Chandrasekhar. The non-linear effect causes a liquid jet to disintegrate into drops with ligaments in between. The sizes of the ligaments decrease with increasing wave-number. The subsequent roll up of the ligament into droplet, the eventual coalescing of the droplet with the main drop and drop oscillation have also been studied.

## 1. Introduction

The study of the capillary instability of a circular liquid jet has been of interest to the fluid dynamicists since the nineteenth century. An earlier account of the work is summarized by Rayleigh (1945). Rayleigh first showed from a linearized stability analysis that neglecting surrounding air, only axisymmetrical surface disturbances with wavelengths greater than the circumference of the jet would grow. The dispersion curve shows that the maximum growth rate occurs at dimensionless wave-number $k = 2\pi R_0/\lambda = 0{\cdot}697$ where $R_0$ is the unperturbed radius and $\lambda$ is the wavelength of the disturbance.

Much experimental and theoretical work has since been done on liquid jet instability. The majority of the work is, however, concerned with the break-up length and break-up time at natural frequency for different flow régimes of velocities, ambient pressures and fluid properties. For liquid jet with moderate speed (typically up to 500 cm/sec), capillary effect dominates jet instability. By assuming that the surface waves grow exponentially at a constant rate during jet break-up, the exponential growth rate can be calculated from the measured break-up time. Both the exponential growth rate calculated this way and the corresponding natural frequency agree qualitatively with Rayleigh's result.

Although Rayleigh introduced the idea of using imposed disturbances to induce jet instability of different frequencies, this idea was not applied by others to study the dispersion curve until recently. Crane, Birch & McCormack (1964,

1965) studied jet instability by using a flexible electronically driven electrical vibrator to introduce disturbances of different wavelengths. Their growth rate deduced from measured break-up time again agreed only qualitatively with Rayleigh's result. They noted the non-sinusoidal behaviour of the surface deformation and attempted to construct a second-order solution to explain the phenomenon. Donnelly & Glaberson (1966) made a careful study of the growth rate of a liquid jet by introducing sinusoidal disturbances of different wavelengths using a loud speaker driven by an audio oscillator. They were the first to attempt to study the growth of the surface waves as a function of time. In the study of the surface disturbance, they chose to measure only the difference between the adjacent neck and swell of the surface deformation. Their results show that the surface waves grow exponentially at a constant rate and the measured growth rate agreed well with the theory of Rayleigh. The agreement is good using the above method of measurement even when the surface wave is definitely non-sinusoidal and grows within one wavelength of the disengagement of the drop from the jet. Thus they concluded that the break-up of the jet was not affected by non-linear effect and that the non-sinusoidal surface deformation was due to the presence of higher harmonics in the vibrating system as was first suggested by Rayleigh. They extended the above measurement to viscous liquid jet and the results again agreed well with the calculation of Chandrasekhar (1961).

For a liquid jet of cylindrical geometry, one can see that mass is conserved for Rayleigh's solution only in first order. Thus, for finite amplitude surface waves, the linearized analysis must break-down. Yuen (1968) calculated the higher-order terms of the surface deformation and showed that the non-sinusoidal surface deformation was indeed a non-linear effect. He also suggested that the agreement between Donnelly & Glaberson's experiment and Rayleigh's linearized theory was due to their method of measurement. A similar calculation was carried out by Wang (1968), although his solution was not uniformly valid for all wave-numbers.

It is clear that all previous experiments on liquid jet instability have not considered non-linear effects in any detail. Although recent non-linear theories give us some insight into the effect of finite amplitude waves on jet instability, as yet there is little understanding of the later stages of the break-up of the jet into droplets of uneven sizes. Thus the aim of this study is to find out in what manner non-linear effects influence the growth of surface waves, the final break-up of a liquid jet and the behaviour of droplets.

The method we chose was to follow photographically a group of waves from the time when the amplitude of the waves was small to the final disintegration of the waves into droplets. To this end we selected the simplest experimental conditions which also conformed as close to the theoretical assumptions as possible. The liquid jet issued vertically downward into the atmosphere. The nozzle was short, so that the velocity profile of the jet was uniform. The speed of the jet was so low that the flow was laminar and the effect of surrounding air was negligible and yet so high that gravitational effect was unimportant. In an effort to impose an axisymmetrical disturbance on the liquid jet, we applied an oscillating voltage between a metal plate concentric with the jet and the jet itself.

The resultant electrostatic force would produce a sinusoidal deformation on the jet surface of the prescribed frequency.

In § 2 we discuss the details of the experimental approach. In § 3 we discuss the experimental results; § 3 is divided into two parts. The first part discusses the growth of the finite surface waves in light of the existing experimental and theoretical results. The second part gives a physical account of the non-linear

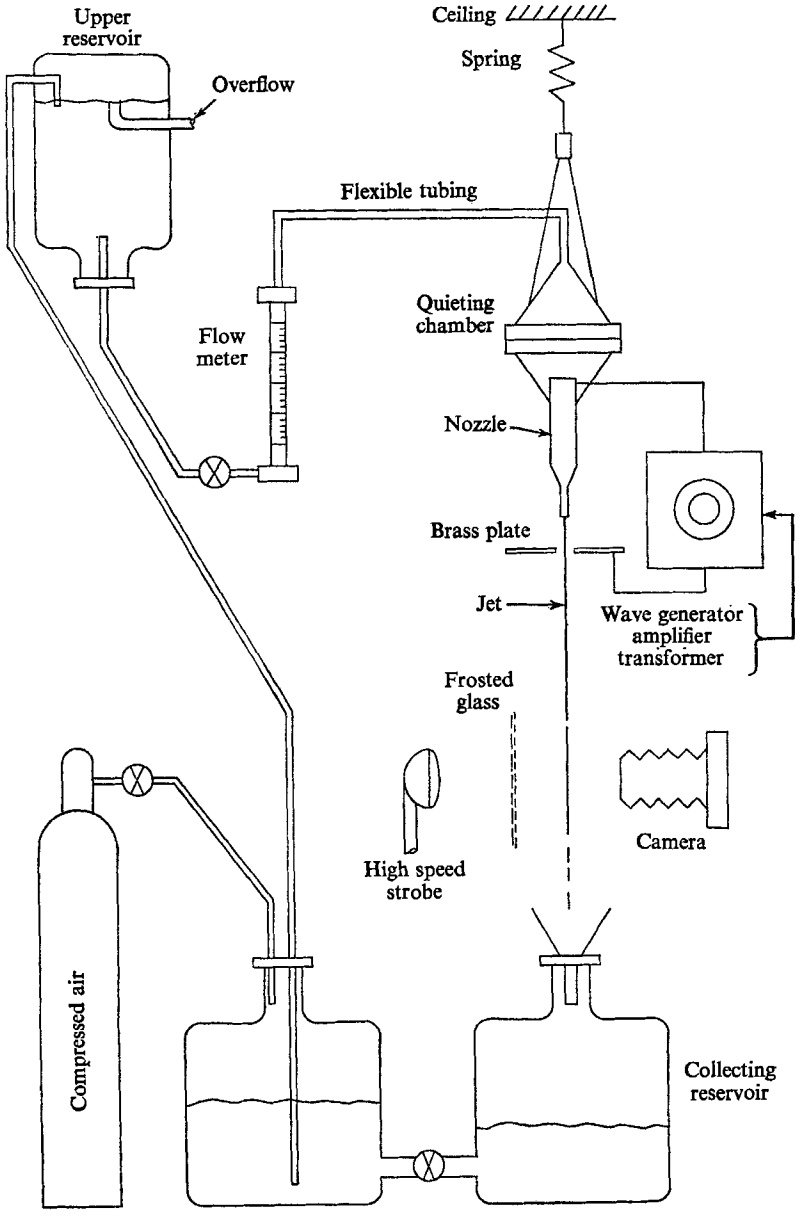


FIGURE 1. Sketch of the apparatus showing principal parts of the experimental arrangement.

effects on the break-up of a liquid jet into drops with ligament in between, the effects of capillary forces and viscosity on the roll-up of the ligament, and finally the coalescing and oscillation of the droplets.

## 2. Experiments

### (i) *Apparatus*

A schematic diagram of the experimental set-up is shown in figure 1. When the apparatus was in operation, distilled water was pumped continuously by air pressure to a constant head (overflow) upper reservoir. Pumping was done by air pressure in order to minimize extraneous vibrations from the mechanical pump. Water from the upper reservoir passed through a flow meter and then through the quieting chamber to a converging nozzle which directed the jet vertically downward into the collecting reservoir.

For viscous glycerin–water solution, the upper reservoir was pressurized with 6 psig air in order to overcome pressure drop and obtain a sufficient jet velocity. In this case the fluid level in the upper reservoir was not constant, but the change in pressure head was small compared to the total driving pressure and the jet velocity remained essentially constant during the experiment.

The quieting chamber consists of two glass funnels epoxied to plexiglass rings fitted with screw holes under an 'O' ring seal for easy assembly. In between the two inverted funnels are several layers of fine mesh screens. The top funnel is filled with $\frac{3}{8}$ in. glass spheres. The spheres together with the screens should damp out any swirling motions created by the lead-in pumping. An air escape valve at the top of the quieting chamber eliminated any trapped air in the chamber.

In order to minimize jet contraction due to gravity, a moderate velocity jet (300–500 cm/sec) was required. Lengthy experimentation with glass nozzles made by drawing heated Pyrex tubing showed a high velocity laminar jet could be created only with a nozzle having very abrupt taper (from 8 mm inside diameter (I.D.) to 2 mm orifice I.D. within an axial distance of 15 mm). Experiments were conducted with nozzles having approximately 1 and 2 mm I.D.

Liquid jet disintegration was found to be very sensitive to external vibrations present in the laboratory floor which found their way to the nozzle. Elimination of these vibrations was accomplished by suspending the quieting chamber and its lead-in hose from soft springs connected to the ceiling. The springs had a 2 sec period of oscillation of the chamber so that any vibrations within the audio-frequency range most likely to affect jet disintegration were prevented from influencing the quieting chamber. As a consequence of this suspension method, jet disintegration under external perturbation was remarkably repeatable and ligament and drop formation details could be observed by stroboscopic illumination with relative ease.

### (ii) *Perturbation*

The induced perturbations on the jet were at audio frequencies and were produced by the conventional method of using a loud speaker or electronically driven vibrator, and also by the electrical forces of an imposed high oscillating voltage. The use of an audio oscillator and amplifier to drive a loud-speaker or a pin

attached to the centre of a vibrator in direct contact with the jet was reported by Donnelly & Glaberson.

In the method of directly using electrical forces, the high voltage electrical signal (typically 300 to 1000 volts) was applied between the jet and a brass plate with a hole concentric with the jet. The thin brass plate was located about $\frac{1}{8}$ in. below the nozzle orifice. The hole was made slightly larger than the jet and its edge was sharpened. The inside of the nozzle was coated with a very thin layer of platinum and electrical connexion was made at the upstream end of the nozzle. In this fashion the electrical forces produced axisymmetric deformations of the jet surface whose amplitude and frequency could be varied by simple adjustments of the power amplifier and signal generator.

For a very viscous jet and for the case with short wavelengths, in order to produce a large enough deformation for observation, it was found necessary to use an electronically driven vibrator having a pin attached to its centre which was brought into direct contact with the jet's surface.

### (iii) *Photography*

Illumination of the jet for visual observation and photography was accomplished by placing a strobotac (General Radio 1538-A) behind the jet and placing a sheet of ground glass between the jet and the strobe, thus backlighting the jet with diffused light. The best photographs were obtained when the ground glass was located 8 in. behind the jet with the camera placed from 1 to 2 ft. in front of the jet.

Single flash photographs were taken with a $4 \times 5$ in. Speed Graphic camera, and high-speed sequences of photographs of the jet were taken with a 70 mm rotating drum camera. These high speed real time sequences of photographs (typically 1000 frames/sec) are possible because the strobe light pulse time duration is extremely short ($0{\cdot}5 \times 10^{-6}$ sec at $\frac{1}{2}$ peak intensity). With such a real time sequence, the growth rate of a swell or neck of a jet could be calculated by measuring the time history of their diameters. Real time sequences were used for all growth rate measurements of water jets and for all ligament and drop formation measurements. Typical single flash photographs are shown in figure 2 (plate 1). Typical real time sequences of photographs are shown in figures 3 and 4 (plates 2 and 3).

The rotating drum camera, manufactured by Southern Instruments, Ltd., Camberley, Surrey, was provided with a trigger switch which closed a relay for the duration of one drum revolution while the drum was rotating. By driving the strobotac with a wave generator through this switch, the strobe could be made to flash at any preset frequency for the duration of one drum revolution, thus acting as a shutter and producing a series of exposures on the film which was wrapped around the drum. In general, from 10 to 30 exposures were obtained on a strip of 70 mm film approximately 21 in. long. The drum rotation speed was determined by the number of photographs desired and by the time taken for that portion of the jet under inspection to travel across the field of view. Because of the extremely short exposure time (1 $\mu$s per photograph) and high strobe flash rates (1000 cps) required for the real time sequences, it became necessary to use two

strobotacs synchronized to flash at precisely the same moment in order to acquire enough light for reasonable photographic exposures. Kodak Tri-X black and white film was used because of its high speed and fine resolution, and the film speed and resolution were increased further by development in Acufine.

(iv) *Surface tension and viscosity measurements*

Surface tension measurements were made with a Cenco Du Nouy Interfacial Tensiometer no. 70545 employing the ring method. Five separate readings of surface tension were taken during each experiment and an average value obtained.

Fluid viscosity measurements were made with nos. 200 and 300 calibrated Cannon–Fenske viscometer pipettes which gave readings of absolute viscosity in centistokes. The pipettes were immersed in a constant temperature bath which was adjusted to the temperature of the jet during each experiment. Adjustments of the bath temperature were necessary because of a temperature change of approximately 2 °F which normally occurred during an experiment. Viscosity measurements were made before, during, and after each run in order to account for these temperature variations and to obtain an averaged value of viscosity.

## 3. Experimental results and discussion

(i) *Growth of surface waves*

In studying the deformation of the surface as a function of time, we followed the same wave using the real time sequences of photographs obtained from the rotating drum camera. This method of data taking differs from that of Donnelly & Glaberson. From the same photograph of the jet such as those shown in figure 2 (plate 1), they measured the successive differences between the neck and the downstream neighbouring swell. The time interval between each of the differences was determined from the vibration frequency.

Measurements of the jet diameters and perturbation wavelengths from the photographic negatives were made with an Excello 8 in. optical comparator capable of accuracy to 0·0001 in. and a magnification factor of 20 times. The time interval between successive photographs in each sequence was determined by the frequency of the illuminating strobotacs. The velocity of the jet was simply determined from the known perturbation frequency and the resultant wavelength measurement.

A typical result of our measurement of water jet with $k = 0{\cdot}408$ is shown in figure 5. In each of the photographs of the real time sequence, both the swell and the adjacent neck one-half a wavelength below the swell were measured. This means that if the swell were measured after it had grown for a time $t$, the neck was measured after it had grown for a time $t + (\lambda/2V)$, where $\lambda$ is the wavelength and $V$ is the jet velocity. In this case, $(\lambda/2V) \simeq 1{\cdot}39 \times 10^{-3}$ sec. Thus in figure 5 the first point for the swell started at time interval 1, the neck from the same photograph started at 2·3. This correction however was found to be insignificant.

The data points in figure 5 are the direct recordings from the film negatives

using the optical comparator. Thus in order to convert to the actual diameter of the jet, the vertical scale should be multiplied by the conversion factor 111·6 mm/in. A smooth curve was best fitted to the data points to minimize the effect of scattering. For further analysis of the data, reading would be taken directly from these curves. The unperturbed jet diameter $D_0$ was calculated by averaging the diameters of a swell and a neck from the smoothed data in the region of small wave amplitude where the waves were more closely sinusoidal. In this case $D_0$ is 1·86 mm. The wavelength is defined as the distance between two swells which is 1·405 cm.

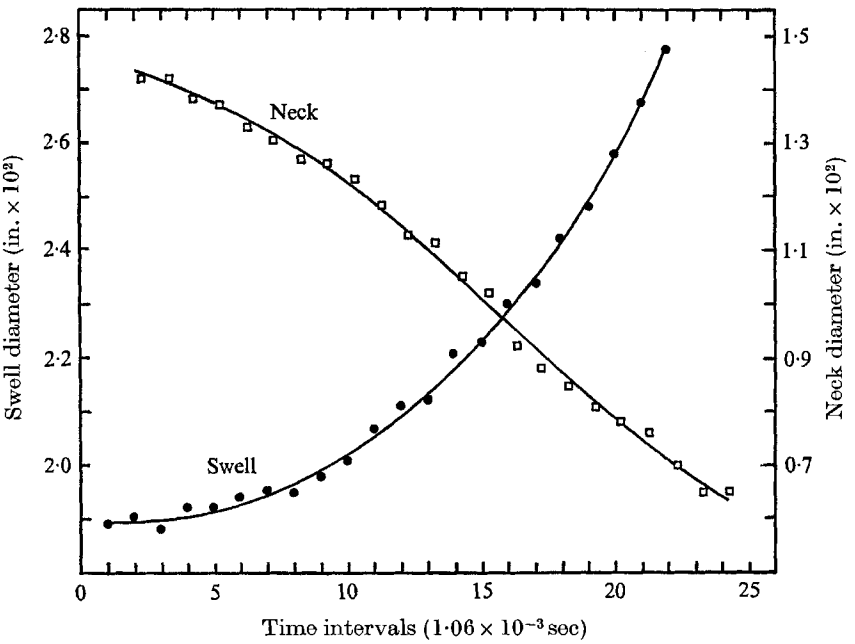


FIGURE 5. Typical measurements of swell and neck diameters *versus* time of a water jet with $T = 59$ dynes/cm, $\lambda = 1{\cdot}405$ cm and $k = 0{\cdot}408$. Actual diameter is obtained by multiplying the vertical scale by the conversion factor, 111·6 mm/in.

Figure 6 shows the result of replotting the data of figure 5. The subscript $s$ denotes swell and $n$ denotes neck. The result of Rayleigh's linearized analysis shows that the exponential growth rate of the instability is a constant. We have therefore plotted in figure 6 the natural logarithm of the actual deformations of swell, neck and the difference between swell and neck as a function of time. The slopes of these curves are the exponential growth rates. The results in figure 6 indicate that the exponential growth rate of both the neck and the swell are not constant, but the exponential growth rate of the difference between the swell and neck remains a constant. The deviation from a straight line of the growth of the swell at early time is small but it exceeds the estimated error of $\pm 0{\cdot}03$ mm. Figure 6 further shows that initially the neck grows faster than the swell. This is a consequence of the conservation of mass for a sinusoidal disturbance. At later time when non-linear effects become important, the swell grows faster than

the neck. Figure 3 (plate 2) shows an example of later stages of growth where the diameter of the neck changes little with time. Even though figure 6 shows part of the curves of both the growth of swell and neck are straight, their slopes are different. They are 91/sec and 78/sec, respectively. Furthermore, both values are higher than the slope of the difference between swell and neck which is 74/sec.

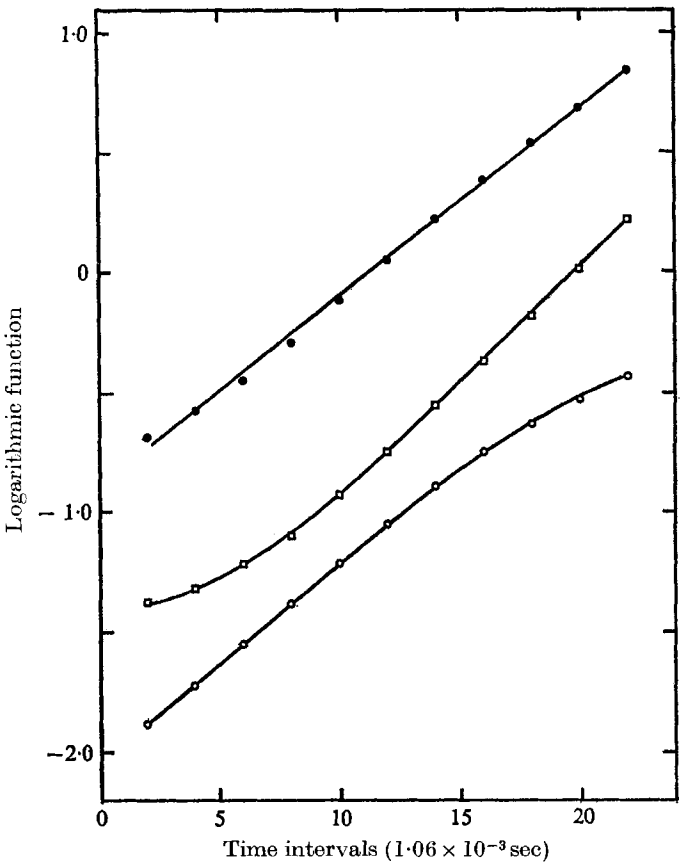


FIGURE 6. Logarithmic plot of data in figure 5 as a function of time with unperturbed jet diameter $D_0 = 1{\cdot}86$ mm. $D_s$ denotes diameter of swell and $D_n$ denotes diameter of neck. ●, $\log_e[D_s(t) - D_n(t)]$; □, $\log_e[D_s(t) - D_0]$; ○, $\log_e[D_0 - D_n(t)]$. The curve of $\log_e[D_0 - D_n(t)]$ has been shifted downward by a scale reading of 0·5.

Similar data taking and analysis were made for water jets of different wavelengths. The result always shows that in general the exponential growth rate of the surface deformation is not a constant. This disagrees with the linearized analysis of Rayleigh but confirms Yuen's analysis that the non-sinusoidal behaviour is a non-linear effect. The exponential growth rate of the difference between the swell and the neck, however, is constant. Evidently the non-linear effects in this case cancel out. This cancelling effect has been noted by Yuen who pointed out that the averaging process using the difference between swell and

neck cancelled the second-order terms in his analysis. Following Donnelly & Glaberson we determined the dispersion curve from the averaging results. This is shown in figure 7 where the exponential growth rate $\omega$ is normalized to $\omega/(T/R_0^3\rho)^{\frac{1}{2}}$, $T$ being the surface tension and $\rho$ the density. The solid curve represents the theoretical calculations of Rayleigh. The absolute agreement is in general good. The scattering of data near $k \simeq 1$ is probably due to the low growth rate and also to the fact that gravitational effect is large where the dispersion curve is steep. For $k > 1$, the present experiment supports the analysis that the liquid jet is stable.

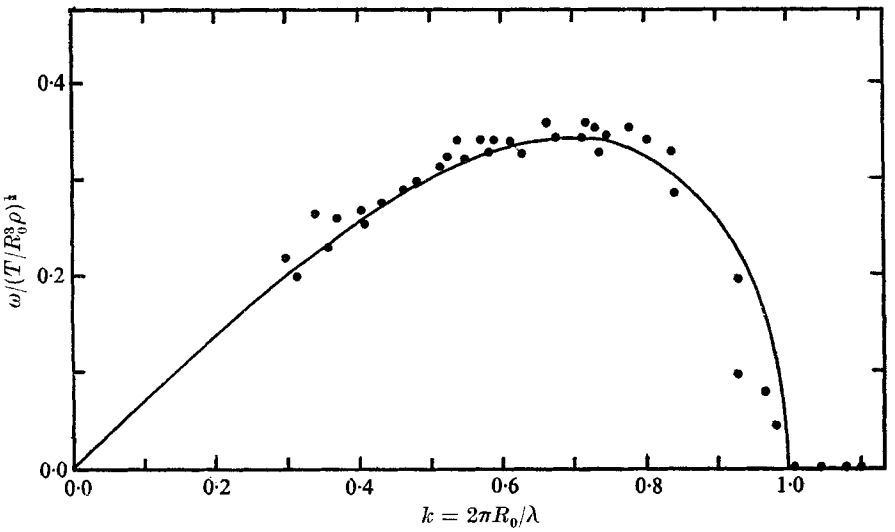


FIGURE 7. Dispersion curve for water jet. The solid line is the theoretical result of Rayleigh's analysis.

No quantitative comparison between Yuen's analysis and experimental results has been attempted. This is because in the analysis the perturbation parameter is based on the initial amplitude of the disturbance which in this case is about 1–2% of the initial diameter, and therefore cannot be measured accurately enough for meaningful comparison. Yuen's analysis predicts that the cut-off wave-number is shifted to $1+\eta_0^2\frac{9}{16}$ as compared to 1 in the linearized case. $\eta_0$ is the initial amplitude of the disturbance. Due to the smallness of $\eta_0$ and the difficulty in accurate measurement of growth rate near $k \simeq 1$, this change in the cut-off wave-number has not been verified. Nor has this experiment observed the shift in wave-number corresponding to maximum growth rate according to Wang's (1968) analysis. Wang shows that the maximum growth rate occurs at $k = 0{\cdot}697 - \eta_0^2\, 3{\cdot}26/4$ as compared to 0·697 in the linear theory. In this case the difficulties seem to be due to $\eta_0$ being infinitesimal and the lack of variation of growth rate near the wave-number of maximum growth as shown in figure 7.

For the case of viscous liquid jet using glycerin–water solution, the same phenomenon occurs. That is, only the average exponential growth rates agree with the linearized analysis of Chandrasekhar (1961). As expected, viscosity

decreases the magnitude of the growth rate. Measurements were made for kinematic viscosity $\nu$ ranging from 0·4 to 1·4 stokes. Figure 8 shows typical experimental results of the average exponential growth rate *versus* wave-number for the case of $\nu = 1{\cdot}22$ stokes and unperturbed radius $R_0 = 0{\cdot}86$ mm. The solid line is the theoretical curve of Chandrasekhar for $J = TR_0/\rho\nu^2 = 2{\cdot}976$. The agreement between theory and experiment is reasonable considering the extreme sensitivity of viscosity coefficient to temperature change. For example, a 2 °F change in temperature causes a 7·6 % change in fluid viscosity and an 11·5 % change in normalized growth rate. The variation of temperature during experimentation was found to be not more than 2 °F. Another factor which contributes to data scattering is that the unperturbed radius varied by as much as 0·05 mm from the average unperturbed radius of 0·86 mm used in the calculation. The shift of the maximum growth rate to smaller $k$ is due to the fact that viscous damping is more effective at larger $k$. Again non-linear effects dominate the surface deformation as shown in photographs *c* and *d* of figure 2.

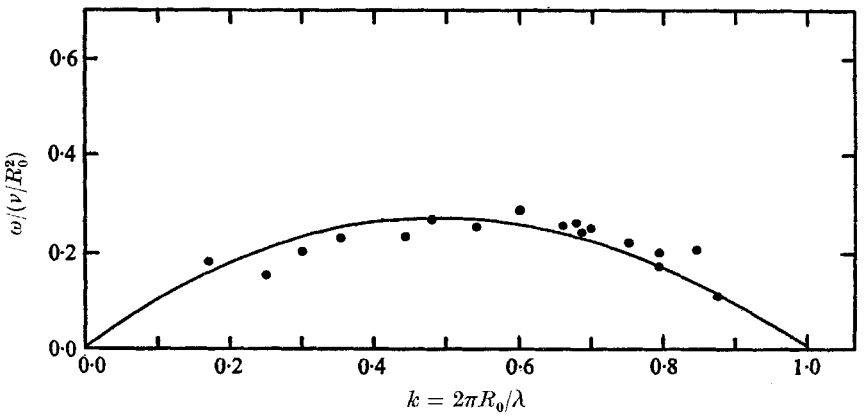


FIGURE 8. Dispersion curve for glycerin–water jet, with $T = 63$ dynes/cm, $\nu = 1{\cdot}22$ stokes and $R = 0{\cdot}86$ mm. The solid line has been taken from Chandrasekhar's monograph with $J = 2{\cdot}976$.

### (ii) *Ligament detachment, drop formation and oscillation*

At the later stages of growth, non-linear effects become very pronounced as shown in the photographs of figures 2–4. For $k$ small, the neck portion of the jet actually stops contracting while the swell portion of the jet is narrowing and growing rapidly. Thus the point of detachment of the jet occurs away from the centre of the neck. The first break-up point to form the ligament always occurs on the downstream end of the ligament. This is because the downstream end has had more time to contract. By analyzing the real time sequence of photographs of the jet, we tried to obtain a better understanding of the final stages of the disintegration into liquid droplets.

Figure 9 shows actual traces of the enlarged photographs of figure 3 starting with photograph (1, 3). The first number in the parentheses denotes the row counting from top to bottom and the second number denotes the column counting from left to right. Thus trace 5 corresponds to photograph (2, 1). From these

traces we can estimate the pressure distribution below the surface. The relationship between pressure and surface configuration is

$$p - p_{\text{atm}} = T\left(\frac{1}{R_1} + \frac{1}{R_2}\right) = T\left\{\frac{1}{R} - \frac{\eta_{zz}}{[1+\eta_z^2]}\right\}\frac{1}{[1+\eta_z^2]^{\frac{1}{2}}}, \tag{3.1}$$

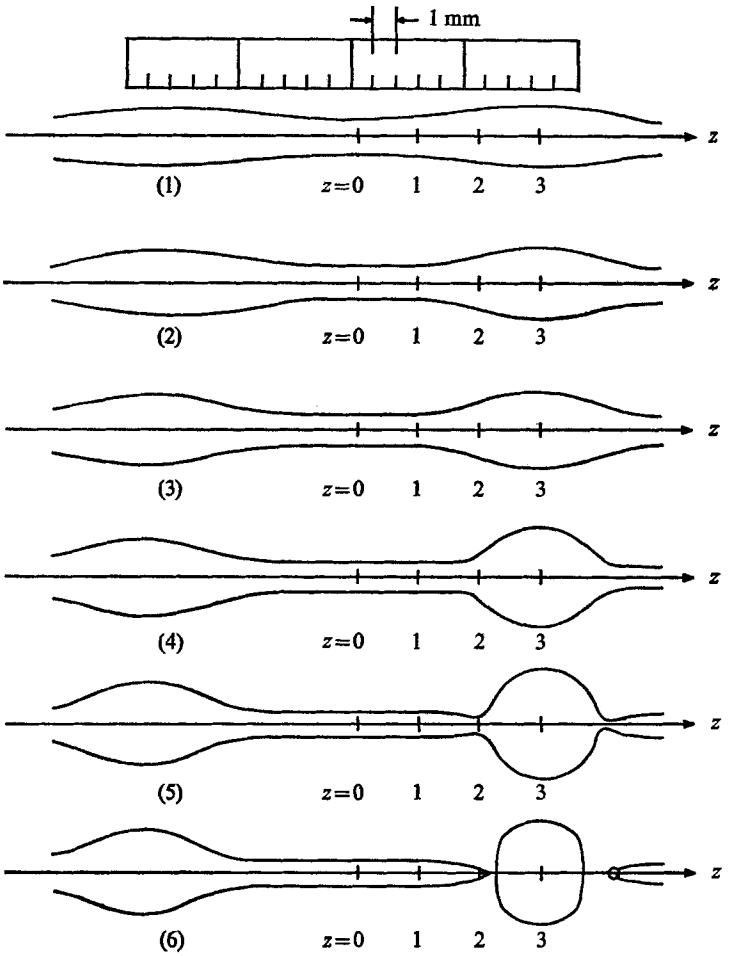


FIGURE 9. Actual traces of the enlarged photographs of figure 3 starting with photograph (1, 3) where the first number in the parentheses denotes row and the second number denotes column.

where $R_1$ and $R_2$ are the principal radii of curvature, $R$ is the radius of the jet, $\eta$ is the surface deformation defined as $R = R_0 + \eta(z, t)$ and the subscript $z$ means differentiation with respect to $z$. A radius of curvature which is concave outward from the jet reduces the internal pressure, and a radius of curvature which is concave inward increases the internal pressure. Using (3.1), the pressure distribution of each of the traces in figure 9 are plotted in figure 10 as a function of the distance $z$. This pressure is the internal pressure of the jet below the surface. If radial velocity and acceleration are negligible, it is also the pressure in the fluid

at the position $z$. Figure 9 shows that the effect of radial velocity and acceleration are probably not important except near position 2. Thus the detail of the pressure peak near position 2 as shown in figure 10 is only qualitatively correct inside the fluid.

Throughout the entire growth process the axial velocity is zero at points $z = 0$ and $z = 3$ from considerations of flow field symmetry. The initial perturbation induces fluid flow away from point 0 in the positive $z$-direction. Non-linear effects then come into play and give rise to the pressure distribution set up at traces 2 and 3 characterized by the strengthening pressure gradient centred at $z = 2$. The strengthening pressure gradient at $z = 2$ implies that a fluid particle at $z = 1$ will move away from point 0 at a much slower rate than a fluid particle at $z = 2$. Therefore fluid particles in the vicinity of $z = 2$ have a much higher velocity gradient than those in the vicinity of $z = 1$ such that a divergence of the velocity is set up in the $z$-direction. Since the fluid is incompressible, the divergence in the $z$-direction must be offset locally by a divergence in the $r$-direction necessitating a contraction of the surface in the vicinity of $z = 2$. Contraction of the surface will occur at $z = 2$ rather than elsewhere because the local divergence in the $z$-direction is larger there than elsewhere.

As the surface contracts the local internal pressure increases and the pressure gradient increases and accelerates the detachment process until the surface contraction creates a maximum point in the pressure distribution (trace 4). The fluid velocity becomes zero at the maximum point and fluid is caused to flow away from this point in both negative and positive $z$-directions, so that complete detachment is effected at $z = 2$. The result of detachment is a sharply pointed ligament whose pressure distribution increases to an extreme value at its point, and a drop whose internal pressure is essentially constant.

The water and viscous jet data show that the size of ligament decreases with increasing disturbance wave-number (see figure 2 (plate 1)). This occurs because non-linear effects diminish as the wave-number increases so that the sinusoidal wave shape is preserved for much larger wave amplitudes as indicated in Yuen's analysis. The ligament of a short wavelength disturbance will therefore grow to a relatively smaller diameter before non-linear effects can create the strong pressure gradient necessary for detachment. This can be seen in photographs *a* and *b* of figure 2 which show that the ligament for $k = 0{\cdot}776$ is much smaller than the ligament for $k = 0{\cdot}323$. The pressure gradient set up by non-linear effects is similar to that depicted at $z = 2$ for trace 3 in figure 10 and the detachment process proceeds in the same manner as that described above.

The viscous jet data reveal that the ligament diameter decreases with increasing fluid viscosity for jets perturbed with the same wave-number. This phenomenon is illustrated in photographs *b* and *c* in figure 2. It originates from the need for an increased pressure difference between the ligament and drop to overcome the dissipative and inhibiting effects of viscosity in order to effect detachment of the ligament from the drop. An increase in viscosity strengthens its inhibiting effects and in order to effect detachment the more slender and threadlike become the ligaments. This can be seen in photograph *d* of figure 2. The effect of increasing viscosity on the ligament-drop pressure distribution of

figure 10 is to increase the difference between the final ligament pressure $P_L$ and final drop pressure $P_D$. The general form of the pressure distribution should remain the same.

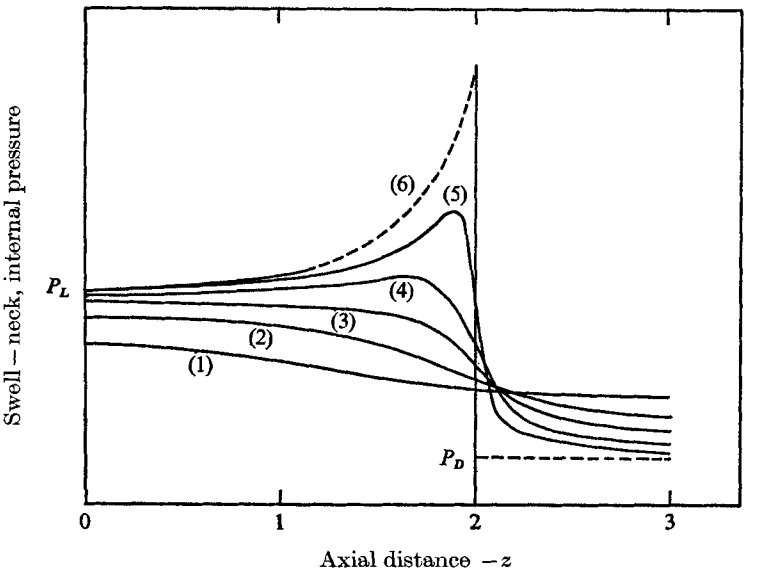


FIGURE 10. Pressure distribution of traces in figure 9. $P_D$ is the drop pressure and $P_L$ is the ligament pressure.

When the ligament detaches from the drop, it begins to contract because it is an unstable configuration. There are two mechanisms causing the contraction.

Initially, the sharply pointed end of the ligament quickly rolls up to form a swell. This can most easily be seen in the viscous case such as shown in figure 3 (plate 2) starting with photograph (2, 4). This is because the internal pressure of the fluid at the pointed end is much higher than the pressure in the uniform cylinder of the ligament. In order to alleviate this pressure differential, the end of the ligament tends to contract to form a swell. From surface tension consideration, for the pressure to be equal, the radius of the swell has to be twice that of the cylinder. The fluid motion will continue, however, because the sphere-cylinder shape is also unstable.

Figure 11 shows some typical measurements of the contractions of ligaments for both water and glycerin–water solutions. The results indicate that the contraction rate for each ligament is a constant. From this experimental fact we can derive the velocity of contraction from simple force-momentum argument. Figure 12 shows the right end of a ligament which is cut at a point of constant radius. The net force acting on the cross-section is the difference between the surface tension force $2\pi RT$ and the net pressure force $\pi R^2(T/R)$. In our simple model of contraction of the ligament, we assume that the fluid in the cylinder is stationary and the fluid in the swell is in motion moving with a velocity $v$. Thus the net force must equal to the net rate of increase of momentum of the swell.

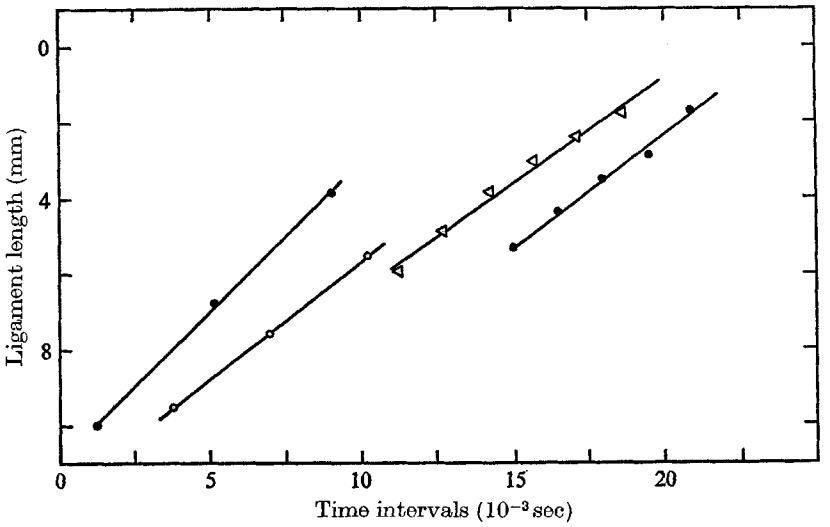


FIGURE 11. Ligament contractions for both water and glycerin–water jets. Data is shown in table 1.

That is,
$$F_{\text{net}} = \frac{d}{dt}(mv) = v\frac{dm}{dt} + m\frac{dv}{dt}, \tag{3.2}$$

where $m$ is the mass of the fluid in the swell. Since the contraction rate is a constant, we further assume that $v$ is a constant and therefore $dv/dt$ is equal to zero in (3.2). This means the increase in momentum is due to the contraction of the swell which swallows up stationary fluid in the cylinder at a rate of $\rho Av$ and imparts on them a velocity $v$. Here $A$ is the cross-sectional area of the cylinder and $D = 2R$. Substituting into (3.2), we have

$$\pi DT = 2\rho Av^2,$$

or
$$v = (2T/\rho D)^{\frac{1}{2}}. \tag{3.3}$$

Since the other end of the ligament also contracts with velocity $v$, the ligament contraction rate $v_L$ is twice this velocity. The exact shape of the swell as shown

| Type of fluid | $\rho$ (g/cm³) | $T$ (dyn/cm) | $\nu$ Stokes | $\lambda$ (cm) | $k$ | Ligament diameter (mm) | Contraction rate: Measured (mm/sec) | Contraction rate: Calculated (mm/sec) |
|---|---|---|---|---|---|---|---|---|
| (*a*) Glycerin–water | 1·26 | 64 | 1·43 | 2·12 | 0·255 | 0·58 | 1000 | 836 |
| (*b*) Glycerin–water | 1·24 | 62 | 1·01 | 2·03 | 0·264 | 0·76 | 760 | 730 |
| (*c*) Water | 1·0 | 59 | 0·01 | 1·23 | 0·441 | 0·68 | 745 | 835 |
| (*d*) Water | 1·0 | 59 | 0·01 | 1·53 | 0·358 | 0·67 | 760 | 844 |

TABLE 1. Comparison of measured and calculated contraction rates of water and glycerin–water ligaments as shown in figure 11.

in figure 12 is not important. Table 1 shows results of both the measured and calculated contraction rates of ligaments of figure 11. The agreement is reasonable considering the crudeness of the calculation.

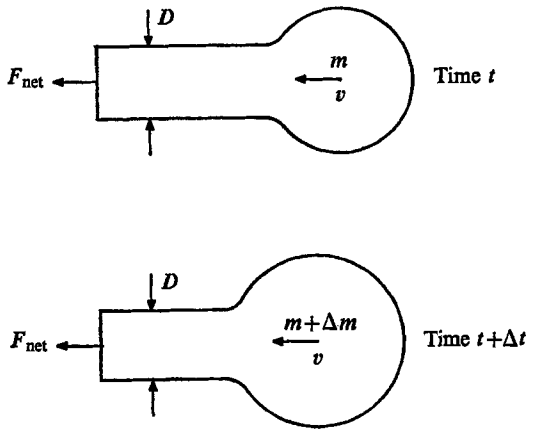


FIGURE 12. Force-momentum balance on the end of a ligament at time $t$ and $t+\Delta t$.

In the case of water ligament, similar processes must occur as in the viscous liquid. In addition, because of the inviscid nature of water as compared to the glycerin–water solution, any disturbance on the surface would tend to propagate as a surface wave. These capillary waves can be seen in both figures 2 and 3 (plates 1 and 2).

Starting with photograph (2, 2) in figure 3, one can see capillary waves are propagating upstream. The photographs show that the wavelengths decrease as distances from the detached end increase. This is because it takes time for the surface waves to travel upstream. Thus the short wavelength waves are caused by the initial contraction of the sharp detached end. As the end rolls up to form larger and larger swell, the disturbance that propagates upstream becomes bigger and its wavelength longer.

These waves have a wavelength smaller than the local circumference of the ligament and should therefore be stable. However, because of the large amplitude of these waves and the contraction of the ligament, a condition can develop such that the pressure at the neck is higher, thus creating an unstable situation. This can be seen in photograph (3, 4) where the first neck of the ligament from the top has a higher pressure than the adjacent swells. Left by itself, fluid would flow away from the neck leading eventually to detachment. In this case the contraction coalesces the two swells together before disengagement at the neck occurs. Thus the high pressure fluid originally at the neck thrusts upward to form a spike as shown in photograph (3, 6). The results of the competition between the contraction and the local disengagement at the neck are not always one-sided. Sometimes a swell is actually detached from the main ligament. This normally occurs for the larger swell at the lower end, where local contraction is slower. An example of this is shown in the second ligament opposite to the

scale reading 6·0 cm in photograph (*b*) of figure 2, where the lower swell has just separated from the main ligament.

Experiments show that soon after the ligament contracts to form a spherule, it will collide with the main drop and coalesce into a bigger drop. This can be seen in photographs (*d*) and (*e*) of figure 2. Photograph (*d*) shows the relative distance between the spherule and the main drop above decreases as they move downward and photograph (*e*) shows the actual coalescence of the two droplets. The collision is due to the fact that the forward end of the ligament was detached first because its growth is in a more advanced stage than at the hinder end. Consequently the ligament remains for a moment connected with the mass behind when it has freed itself from the mass in front; and thus the resultant spherule acquires a relative backward momentum, which of necessity leads to collision. The collision is also facilitated by the higher drag to weight ratio of the spherule. In some instances, upon collision, the spherule would rebound and subsequently coalesce. We have not studied this in any detail.

The detached drops into which a jet is ultimately resolved do not at once assume and retain a perfectly spherical form, but execute a series of oscillations, being alternately compressed and elongated in the direction of the axis of symmetry. Photograph (*e*) of figure 2 shows a typical drop oscillation of a water jet. The period of oscillation agrees well with the calculation of Lamb (1932) assuming only infinitesimally deformed shape. All the glycerin–water jets fall into the category of aperiodic damped solution of Reid (1960) as can be seen in photographs (*c*) and (*d*) of figure 2.

## 4. Summary

This study has led to a more precise description of the disintegration of a liquid jet into droplets. It is found in general that non-linear effects dominate the break-up processes, particularly at small wave-number. During the course of experimentation, we have found it helpful to look at capillary instability in the following way. For a circular liquid column, the pressure inside is higher than the ambient pressure by the surface tension times the inverse of the radius of curvature. Thus, when the liquid jet is disturbed, the pressure at the swell is decreased by an increase in the radius of the cross-section. This decrease, however, is opposed by an increase in pressure due to the concave curvature in the axial direction. The opposite is true in the neck region. The net result is that only for certain wavelengths does the deformed surface cause a net increase in pressure at the neck and a decrease in pressure at the swell. This induced pressure gradient would cause the fluid to flow from the neck to the swell, thus enhancing the instability. The advantage of this point of view is that we can trace the curvatures from the photographs. Thus, the time history of the pressure distribution would allow us to get a better understanding of the later stages of the disintegration of a liquid jet.

Measurements of the growth of finite surface waves show that the non-sinusoidal shape of the deformed surface is a non-linear effect. The neck initially grows faster than the swell but at later stages the trend tends to reverse itself.

The non-linear effect is especially pronounced at small wave-number. The average growth rate of the swell and neck, however, agrees well with the linearized analysis. The viscous fluid of water–glycerin solution behaves similarly. As expected, viscous damping causes the growth rate to be lower and the maximum growth rate to shift to lower wave-number. The present experiment on a water jet is not accurate enough to confirm the shifts in the cut-off wave-number and the wave-number of maximum growth as predicted by the non-linear theories.

The analysis of the photographs shows that at later stages of growth non-linear effects cause a pressure gradient in the axial direction such that the flux of fluid out of the neck is smaller than the flux of fluid into the swell. This forces the surface in between the neck and swell to contract in order to satisfy mass conservation. The configuration of this local depression is, however, unstable. The net result is that the point of separation occurs away from the neck and the neck portion of the liquid column becomes the ligament. It is found that the size of the ligament increases with decreasing wave-number.

The principal feature in the roll-up of the ligament is that the only stable configuration is that of a sphere. Thus, in the beginning, the two pointed ends of the ligament contract to form two swells in an effort to equalize the pressure distribution. This hemispherical-cylinder arrangement is, however, not an equilibrium configuration. Thus, both ends approach each other lastly to form a spherical drop. In the case of water which is nearly inviscid, the picture is complicated by the appearance of capillary surface waves. These finite-amplitude waves can cause local instability and in some cases even cause break-up of the ligament.

Finally, some observations have been made on the coalescing of the spherule with the larger drop and the subsequent oscillation of the droplets. The period of oscillation for water is found to agree well with Lamb's calculation.

The authors thank Professor R. S. Tankin for many helpful discussions. This research was supported by the National Science Foundation under Grant GK-1600.

## REFERENCES

CHANDRASEKHAR, S. 1961 *Hydrodynamic and Hydromagnetic Stability*. Oxford: Clarendon Press.

CRANE, L., BIRCH, S. & MCCORMACK, P. O. 1964 The effect of mechanical vibration on the break-up of a cylindrical water jet in air. *Brit. J. Appl. Phys.* **15**, 743–750.

CRANE, L., BIRCH, S. & MCCORMACK, P. O. 1965 An experimental and theoretical analysis of cylindrical liquid jets subjected to vibration. *Br. J. Appl. Phys.* **16**, 395–408.

DONNELLY, R. J. & GLABERSON, W. 1966 Experiment on capillary instability of a liquid jet. *Proc. Roy. Soc. Lond.* A **290**, 547–556.

LAMB, H. 1932 *Hydrodynamics* (6th ed.). New York: Dover.

RAYLEIGH, LORD 1945 *The Theory of Sound*, vol. II (2nd ed.). New York: Dover.

REID, W. H. 1960 The oscillations of a viscous liquid drop. *Quart. Appl. Math.* **18**, 86–89.

WANG, D. P. 1968 Finite amplitude effect on the stability of a jet of circular cross-section. *J. Fluid Mech.* **34**, 299–313.

YUEN, M. C. 1968 Non-linear capillary instability of a liquid jet. *J. Fluid Mech.* **33**, 151–163.

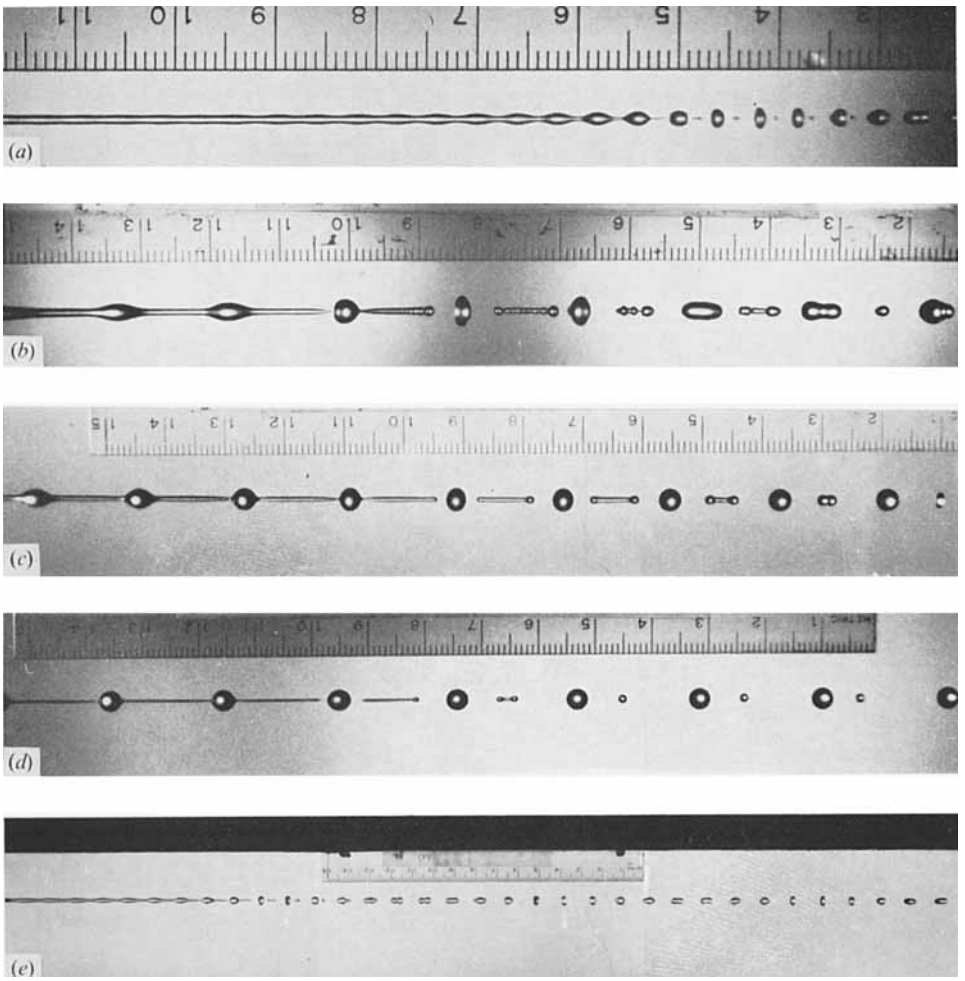


FIGURE 2. Typical photographs of liquid jets. (*a*) Water, $\lambda = 0{\cdot}406$ cm, $k = 0{\cdot}776$. (*b*) Water, $\lambda = 1{\cdot}70$ cm, $k = 0{\cdot}323$. (*c*) Glycerin–water, $\lambda = 1{\cdot}81$ cm, $k = 0{\cdot}307$, $\nu = 1{\cdot}01$ stokes. (*d*) Glycerin–water, $\lambda = 2{\cdot}12$ cm, $k = 0{\cdot}255$, $\nu = 1{\cdot}43$ stokes. (*e*) Water, $\lambda = 1{\cdot}32$ cm, $k = 0{\cdot}428$. Drop oscillation: measured period = 0·0279 sec, calculated period = 0·0248 sec.

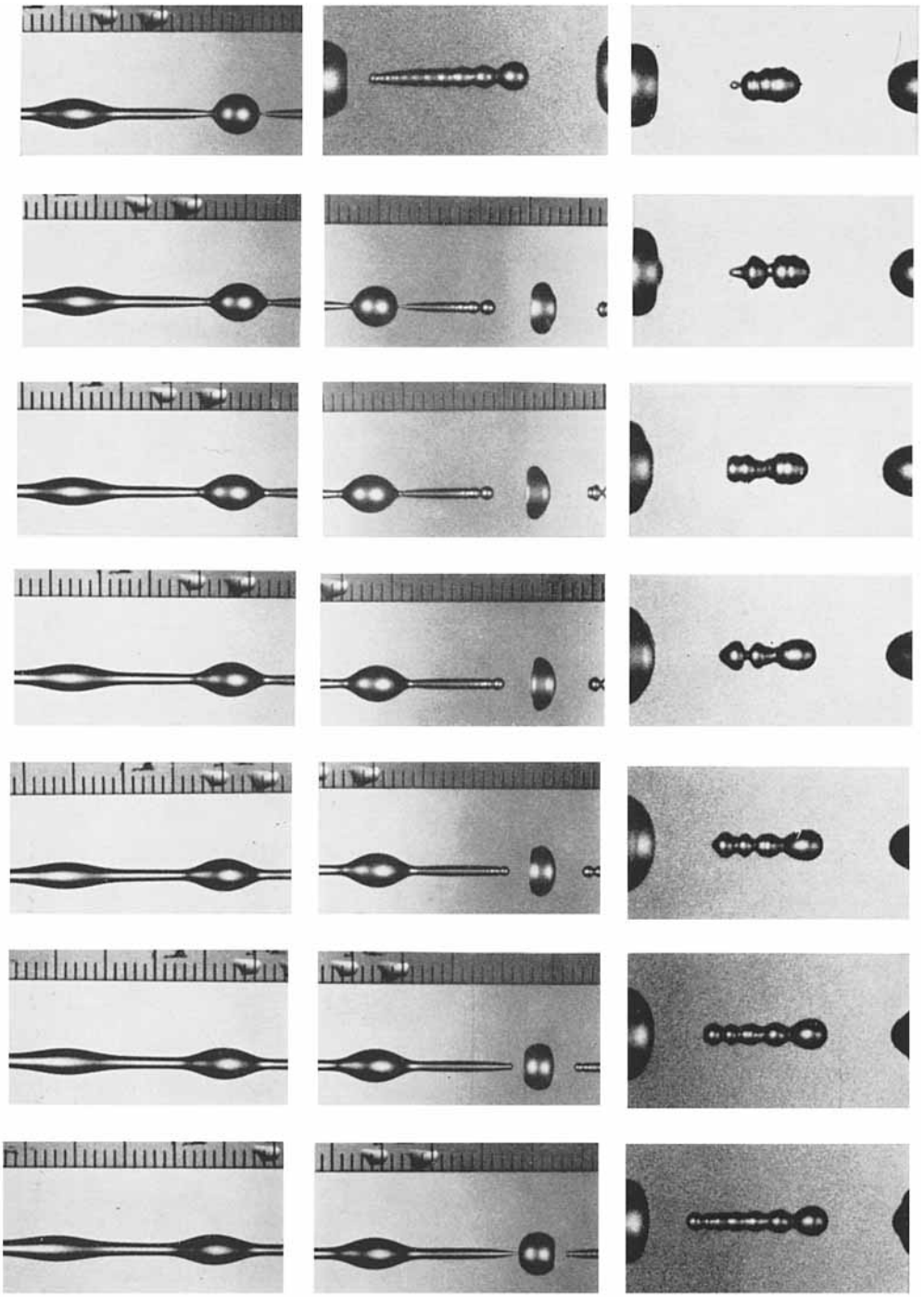

FIGURE 3. Real time sequence of photographs of water jet break-up with $\lambda = 1{\cdot}53$ cm, $k = 0{\cdot}43$ and $T = 59$ dynes/cm. Time interval between each photograph is $1{\cdot}25 \times 10^{-3}$ sec. Time increases from left to right, top to bottom.

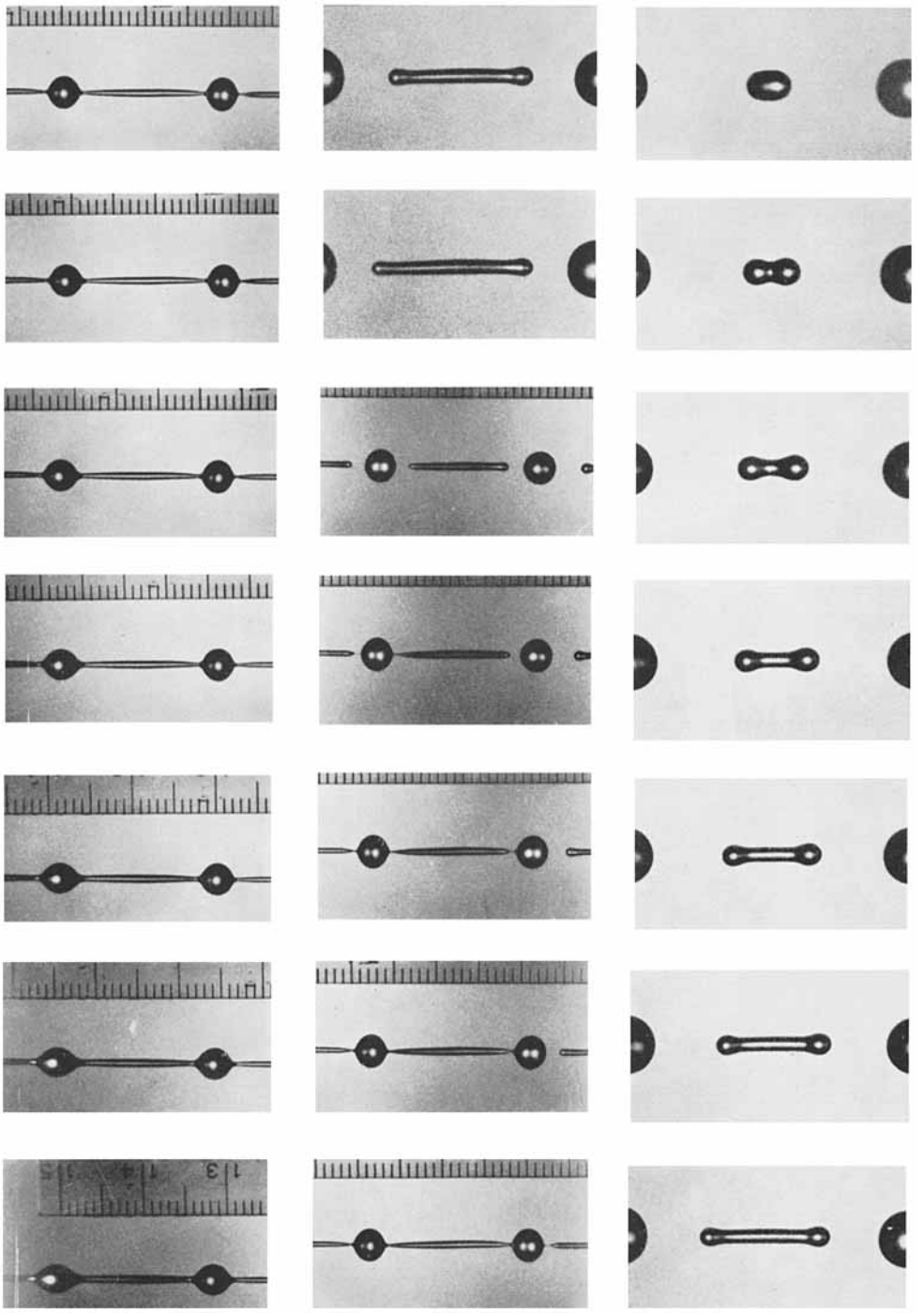

FIGURE 4. Real time sequence of photographs of glycerin–water jet break-up with $\lambda = 1{\cdot}89$ cm, $k = 0{\cdot}294$, $T = 61$ dynes/cm, $\nu = 0{\cdot}56$ stokes. Time interval between each photograph is $2{\cdot}08 \times 10^{-3}$ sec. Time increases from left to right, top to bottom.